Chapter 7

Discontinuities of the mantle transition zone

7.1 Nature of the mantle transition zone

The mantle transition zone marks the transition from the upper to the lower mantle. Its characteristics are important for our understanding of Earth's dynamics. The mantle transition zone is bounded by distinct seismic discontinuities which are named after the average depth in which they occur: the 410-km discontinuity or '410' (*Jeffreys*, 1936), and the 660-km discontinuity or '660' (*Niazi and Anderson*, 1965). Over the past decades, a number of seismic studies have demonstrated the global existence of these discontinuities and have mapped their topography (e.g. *Shearer and Masters*, 1992; *Flanagan and Shearer*, 1998a; *Gossler and Kind*, 1996; *Gu et al.*, 1998). However, the '410' is usually more difficult to detect than the '660' due to its smaller velocity contrast and to a regional strong topography, which makes observations in long period data rather difficult (*Bina and Helffrich*, 1994; *Rost and Weber*, 2002; *Flanagan and Shearer*, 1998b).

Furthermore, a weaker discontinuity at 520 km depth ('520') has been observed locally. However, a global existence of the '520' is still a matter of controversial discussion. Some studies claim that the 520-km discontinuity is a global feature (*Shearer*, 1990, 1996; *Gaherty et al.*, 1999), whereas others find that it can be observed only in certain regions (*Gossler and Kind*, 1996; *Deuss and Woodhouse*, 2001), or that it is not found beneath continental shields (*Gu et al.*, 1998), or that it might not exist at all (e.g. *Cummins et al.*, 1992; *Bock,* 1994).

According to the *IASP91* velocity model (*Kennett*, 1991; *Kennet and Engdahl*, 1991), the velocity increase at the '410' is +3.6% for *P* waves and +4.1% for *S* waves. At the '660' it is +5.8% for *P* waves and +6.3% for *S* waves. For the '520', *Helffrich* (2000) reports a velocity contrast of only 1% or less, and *Bock* (1994) used an impedance contrast of 2% and assumed a second-order seismic discontinuity between 510 and 530 km for calculating synthetic seismograms.

The two main seismic discontinuities in the mantle at 410 and 660 km depth are most probably pressure-induced phase transformations in peridotite rather than a change in chemical composition. Experiments in the mid-1960s (*Ringwood and Major*, 1966) showed that the olivine component of peridotite undergoes successive pressure-dependent transformations: at pressures of 13-14 GPa (corresponding to 410 km depth), olivine transforms into wadsleyite, at pressures of 18 GPa (corresponding to 520 km depth) wadsleyite transforms into ringwoodite, which ultimately breaks down to form perovskite

and magnesiowüstite at pressures of about 23 GPa, corresponding to 660 km depth in the Earth (*Bina and Helffrich*, 1994; *Helffrich*, 2000; *Helffrich and Wood*, 2001). High-pressure mineral-physics studies have shown that transition zone minerals at average mantle temperatures have anomalously high water solubility relative to upper-mantle minerals. Water solubility of the mantle transition zone is about 10-30 times higher than that in the upper and probably lower mantles (*Bercovici and Karato*, 2003).

The transformations at the '410' and '520' have positive Clapeyron slopes, with d*P*/d*T* of approximately +3 MPa K^{-1} and +4 MPa K^{-1}, respectively. In contrast, the breakdown of ringwoodite to perovskite plus magnesiowüstite at the '660' has a negative slope of -2 MPa K^{-1} (*Helffrich*, 2000). Thus, if the 410- and 660-km discontinuities are entirely due to these phase transformations, regions of abnormally low temperature such as subduction zones should correspond to elevation of the '410' to lower depths and depression of the '660' to greater depths (Figure 7.1). In general, the '660' is depressed under cold regions (slabs) as expected, but the '410' appears to be far more complicated (*Gu et al.*, 2003; *Flanagan and Shearer*, 1998a,b). The stacked *P*-to-*S* converted phase (receiver function) from the '410' may be rather weak and complicated and sometimes shows negative pulses above the '410' (*Gilbert et al.*, 2003; *Song et al.*, 2004).

However, these discontinuities due to phase transitions are not sharp boundaries but rather gradual transitions. This is due to a coexistence zone of the two mineral phases at each transition (*Helffrich*, 2000), furthermore to the influence of temperature and water content. From short period data, the thickness of the '410' was estimated to be about 5 km (*Yamazaki and Hirahara*, 1994; *Helffrich*, 2000). The '660' is also thought to be less than 10 km thick (*Castle and Creager*, 2000). The 520-km discontinuity does not reflect shorter period energy (*Benz and Vidale*, 1993) and is therefore probably a boundary spread over at

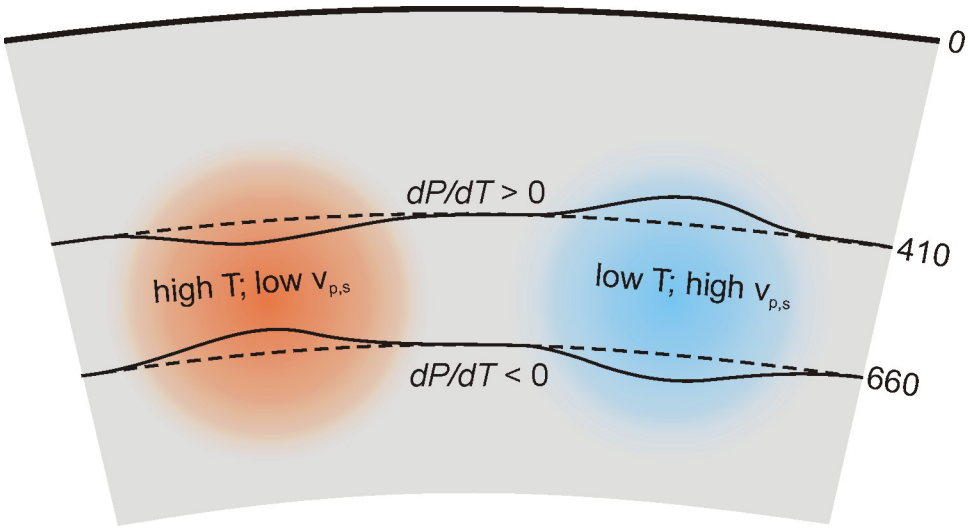

Figure 7.1: Schematic depiction of the mantle transition zone in an olivine-dominant mantle after *Lebedev et al.* (2002). The transition from olivine to wadsleyite and from spinel to perovskite and magnesiowüstite give rise to the 410- and 660-km discontinuities, respectively. The effective Clapeyron slopes *dP/dT* have opposite signs. Absent lateral variations in composition, relatively low temperatures (T) cause thickening of the transition zone and increase in seismic velocities (v_p, v_s), while high temperatures cause thinning of the transition zone and decrease in v_p and v_s.

least 10 km in depth.

The non-olivine component in the mantle is about 30%. Phase changes in the pyroxene and garnet components of mantle peridotite are gradual, and lead to changes in slope of the curves of seismic velocity versus depth rather than discrete discontinuities (*Helffrich and Wood*, 2001) and/or to multiple discontinuities especially in the lower part of the mantle transition zone (e.g. *Akaogi et al.*, 2002; *Simmons and Gurrola*, 2000; *Deuss and Woodhouse*, 2001).

7.2 Observation of the upper mantle discontinuities in the study area

In order to investigate the '410' and '660' with the receiver function data, it is necessary to take into account that due to the ray geometry, the obtained information stem from a region 80-170 km ('410') and 150-310 km ('660') away from the receiver. Therefore, the piercing points of the rays at depth interfaces of 410 km and 660 km were plotted (Figure 7.2). The data comprise more than 5500 receiver functions that can be used for investigating the upper mantle discontinuities. As most events were recorded from northeastern directions, the area northeast of the western Bohemian Massif, between Berlin and Prague, is sampled best. Nevertheless, there is still a fairly good data coverage beneath the western Bohemian Massif and west of it. To the south, there is a data gap especially in the piercing points at 660 km depth.

The amplitudes of *Ps* conversions from the upper mantle discontinuities are about four times weaker than the Moho *Ps* conversion signal. Hence it is necessary to stack individual traces in order to enhance the signals from the '410' and '660'. Therefore the area was divided into 43 non-overlapping boxes of $1° \times 1°$, which corresponds to approximately 70 km (E-W) × 112 km (N-S) at the surface (Figure 7.2). The data were corrected for distance moveout and stacked according to the distribution of piercing points within the boxes at 410 km and 660 km depth, respectively. Data examples for two boxes are given in Figures 7.3 and 7.4 for the '410' and '660'. Different filters were tested beforehand in order to enhance the signals of the '410' and '660'. This led to the choice of a bandpass filter between 2-20 s.

Figure 7.5 shows the receiver function data sorted by piercing points at 410 km depth and stacked for each box that contains at least 25 traces. Table 7.1 gives the values of measured delay time and difference to the delay time predicted by the reference model *IASP91*. The measured delay times vary between 44.0 and 45.6 s between individual boxes (see Table 7.1). Especially the southernmost boxes (numbers 37 to 41) show significantly increased delay times of 44.8 to 45.6 s. However, the data coverage in the southern boxes is not as dense as in most of the other boxes, which makes the observation less stable. The sum trace of all individual traces shows the *Ps* conversion signal from the '410' at 44.8 s, which is 0.7 s later than predicted by the *IASP91* reference model.

A similar image is given in Figure 7.6 for the traces with piercing points at 660 km depth, which means that the same data were sorted in a different manner than for the discontinuity at 410 km depth. Here the delay times of individual boxes vary between 67.6 and 71.0 s (see Table 7.1). Like for the '410', the southernmost boxes (numbers 36 to 42) show the largest delay times of 69.6 to 71.0 s while the data coverage is clearly less than in most of the other boxes.

Furthermore, a signal at 54.4 s delay time, which may be attributed to the discontinuity at 520 km depth is visible in the sum trace of Figures 7.5 and 7.6 (sum traces are identical as the same set of individual traces is stacked). The signal can be followed through most of the individual boxes and appears to be rather coherent.

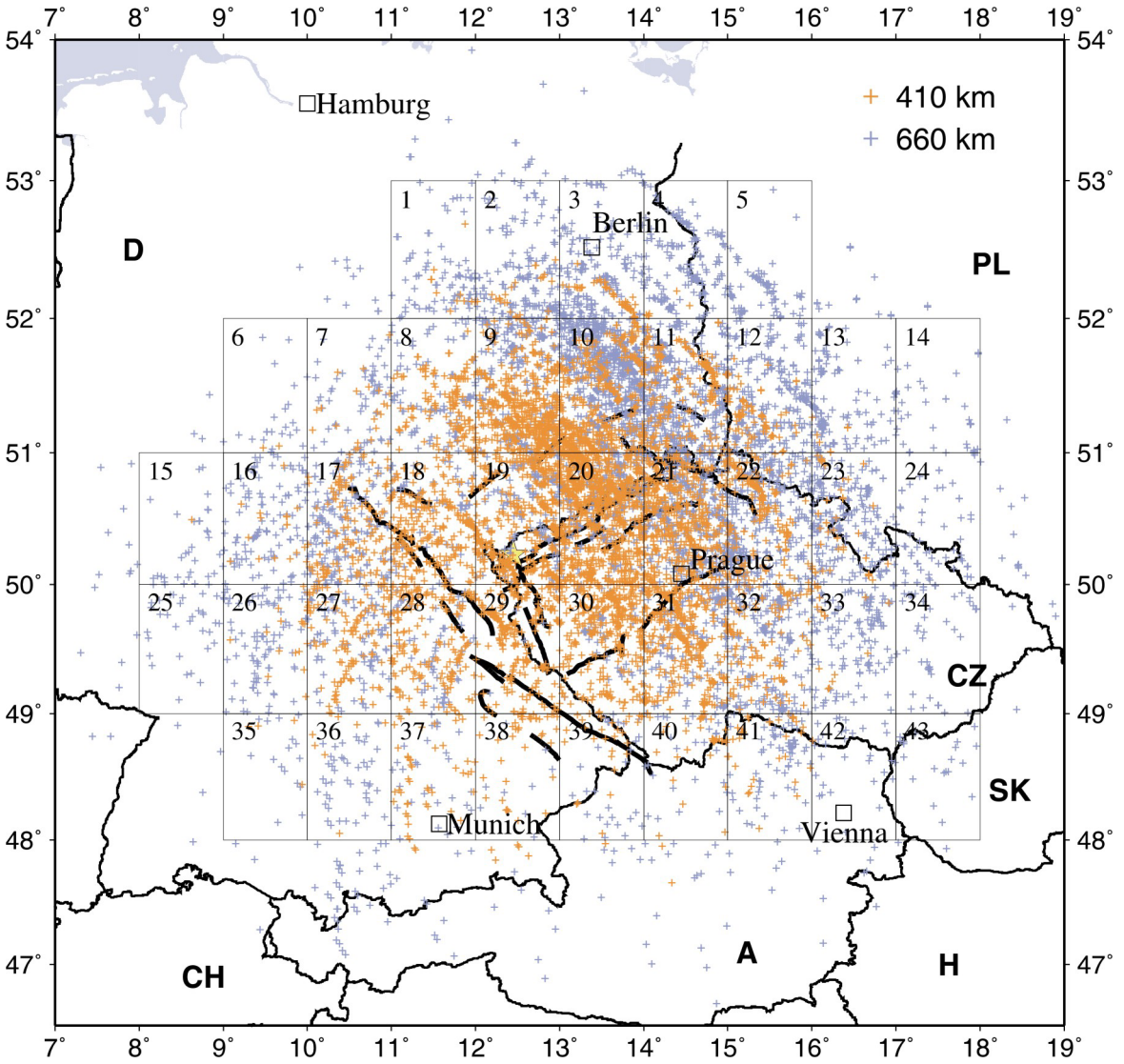

Figure 7.2: Piercing points of the *P*-to-*S* converted phases at interfaces at 410 km (orange) and 660 km depth (blue). The piercing points are located 80-170 km and 150-310 km away from the recording station for the 410- and 660-km discontinuity, respectively. For both depth values the same division of the area into boxes of 1°×1° was chosen. Hence, the boxes are sampled by different numbers and locations of piercing points at 410 and 660 km deep interfaces.

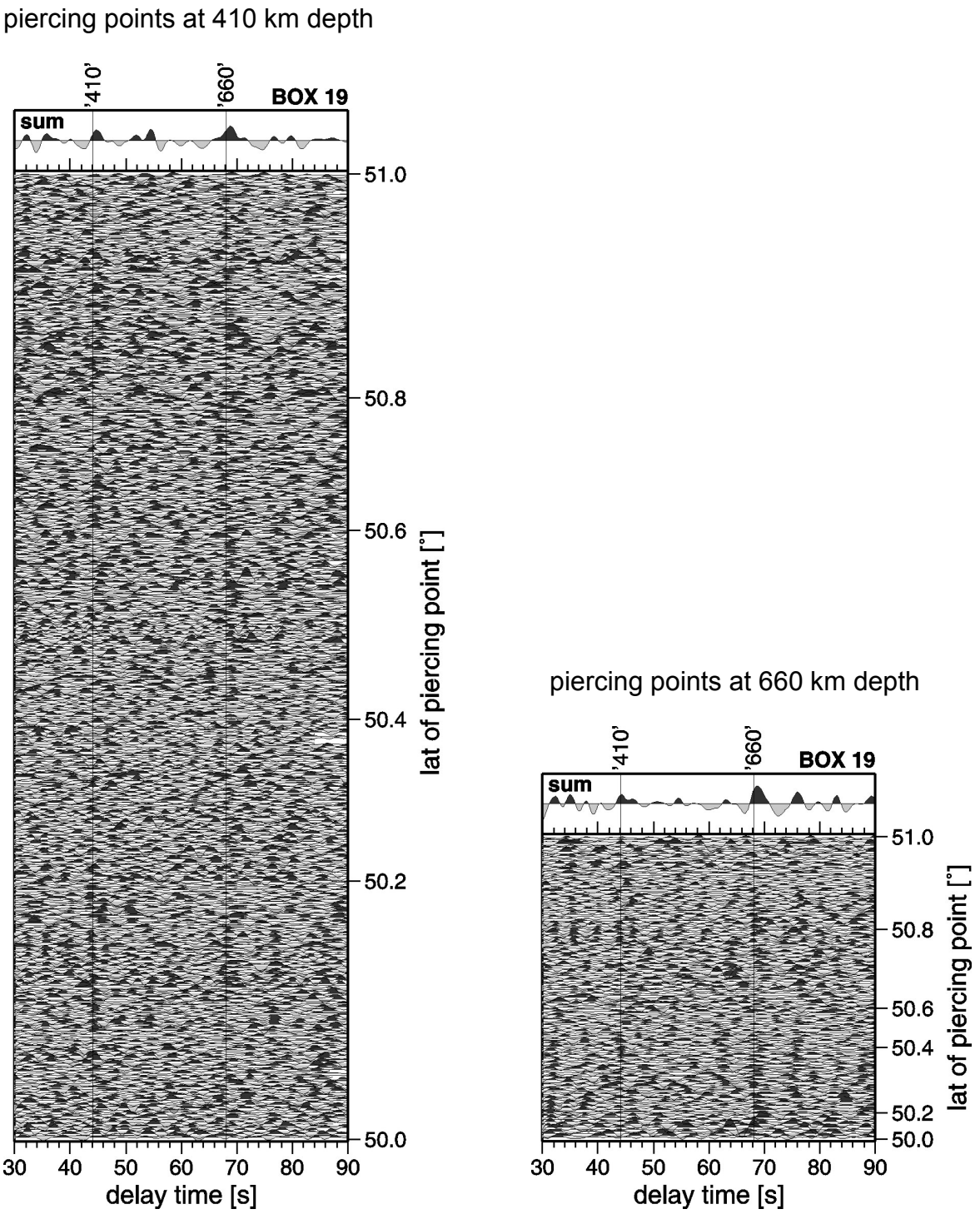

Figure 7.3: Data example (Box 19) in the time window between 30 to 90 s after the *P* onset. For different depth layers, the data gathered within the same box is different. **Left**: traces were sorted according to piercing points at 410 km depth. **Right**: traces were sorted according to piercing points at 660 km depth.
Single traces were filtered between 2-20 s, moveout-corrected and stacked. On top of the single traces, the sum trace is displayed. The *Ps* conversion signals from the 410- and 660-km discontinuities are rather weak in the single traces but clear in the sum trace.

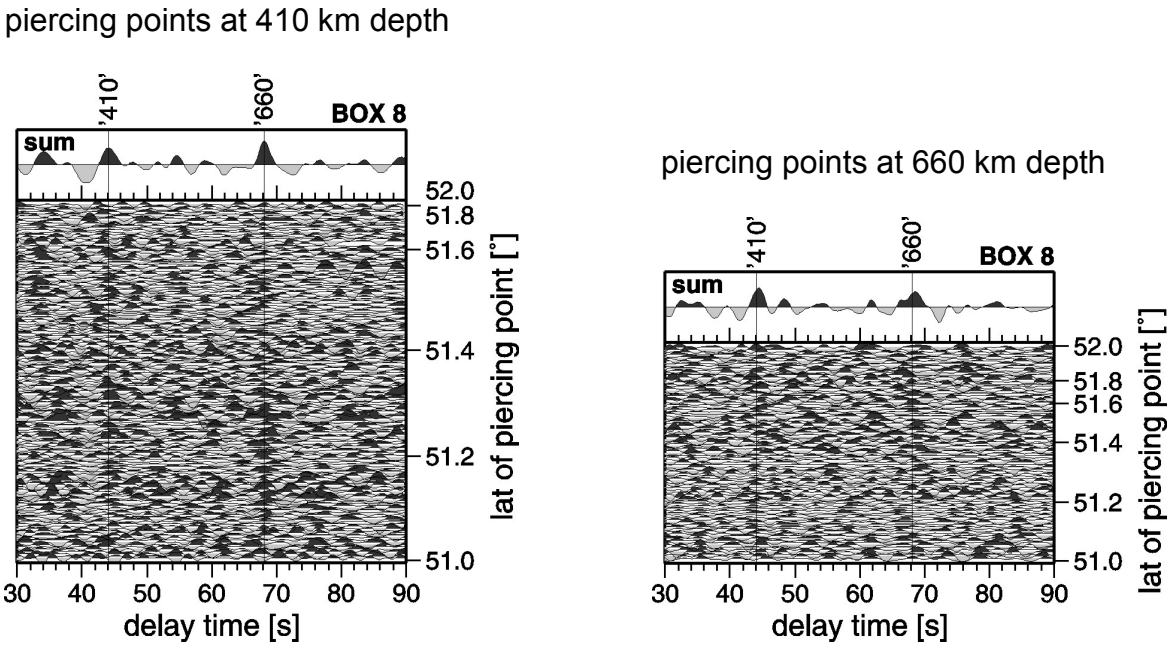

Figure 7.4: Data example (Box 08) in the time window between 30 to 90 s after the *P* onset. For different depth layers, the data gathered within the same box is different. **Left**: traces were sorted according to piercing points at 410 km depth. **Right**: traces were sorted according to piercing points at 660 km depth. The single traces were processed as described in Figure 7.3.

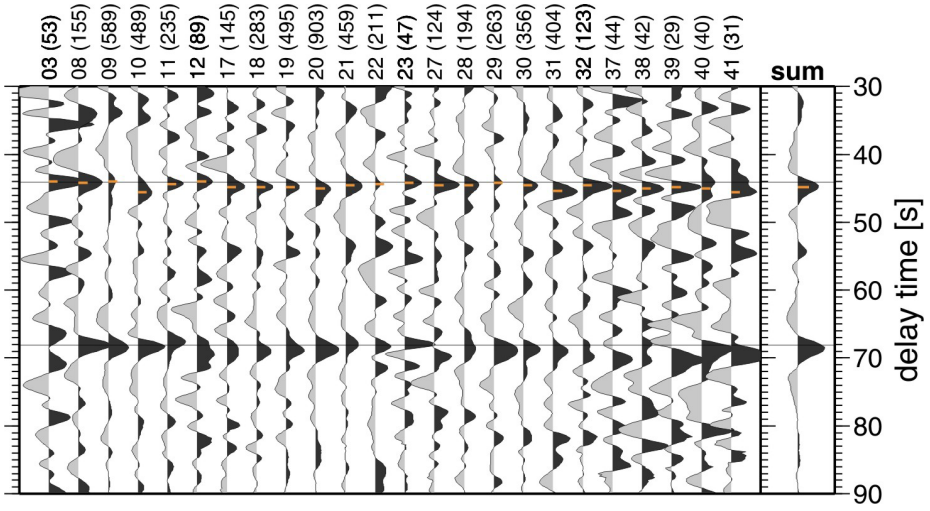

Figure 7.5: Stacked receiver functions of boxes containing at least 25 traces with piercing points at 410 km depth. The stacked traces are sorted by box number, the vertical ordinate shows the delay time with respect to the *P* onset. On top of each trace, the box number and, in brackets, the number of stacked traces are given. The single traces were moveout-corrected and filtered between 2-20 s before stacking. On the right of the Figure, the sum trace of all boxes is given. Lines at 44.1 s and 68.1 s mark the delay times of the 410- and 660-km discontinuities according to the *IASP91* reference model. Coherent positive arrivals near the delay times predicted by *IASP91* are clearly visible for both the '410' and '660'. The orange dash shows the delay time of the '410' that was picked for each box and for the sum trace. Most boxes display slightly longer delay times than predicted by *IASP91*. In the sum trace, the delay of the signal from the '410' is 44.8 s, i.e. 0.7 s later than predicted by *IASP91*. Furthermore, at 54.4 s delay time, a signal attributed to the 520-km discontinuitiy (not included in *IASP91* model) is visible in the sum trace and can be followed through most of the boxes.

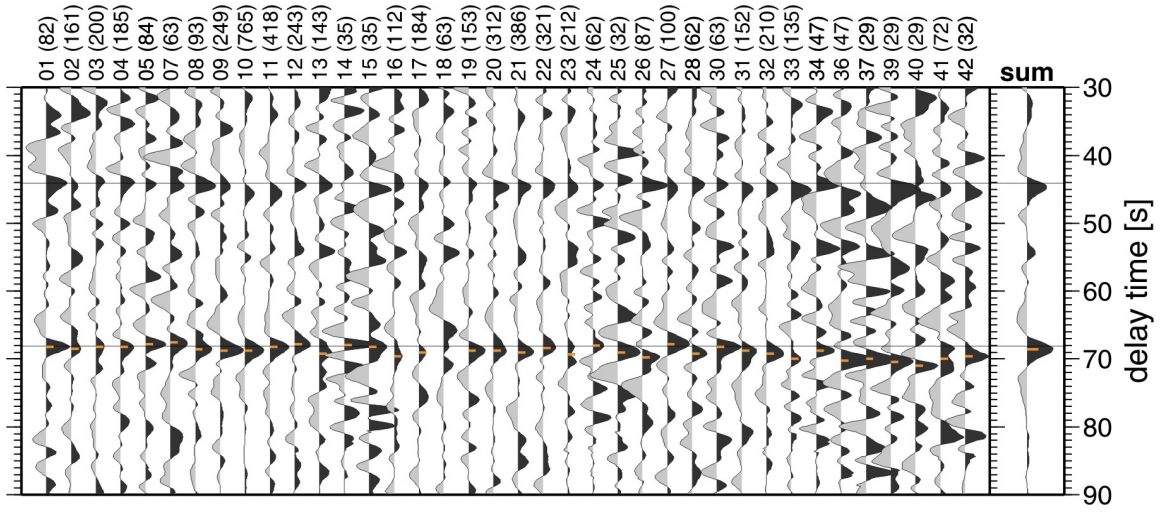

Figure 7.6: Same as Figure 7.4, but single traces were sorted by their piercing points at 660 km depth. The orange dash shows the delay time of the '660' that was picked for each box and for the sum trace. As for the 410-km discontinuity, most boxes display slightly longer delay times than predicted by *IASP91*. In the sum trace, the delay of the signal from the '660' is 68.6 s, i.e. 0.5 s later than predicted by *IASP91*. As in Figure 7.4, a signal from the discontinuity at 520 km depth is visible in the sum trace at 54.4 s delay time and in many boxes.

Table 7.1: Box number, number n of stacked traces for each box for the '410' and '660', delay times of the *Ps* conversions $t_{Ps,410}$ and $t_{Ps,660}$ and delay time difference for the conversions from the two discontinuities within each box.

Box №	n ('410')	n ('660')	$t_{Ps,410}$ [s]	$t_{Ps,660}$ [s]	($t_{Ps,660}$-$t_{Ps,410}$) [s]
1	11	82	-	68.2	-
2	24	161	-	68.5	-
3	53	200	44.0	68.2	24.2
4	6	185	-	68.2	-
5	0	84	-	67.8	-
6	2	22	-	-	-
7	22	63	-	67.6	-
8	155	93	44.2	68.6	24.4
9	589	249	44.0	68.8	24.8
10	489	765	45.6	68.8	23.2
11	235	418	44.4	68.2	23.8
12	89	243	44.0	67.8	23.8
13	8	143	-	69.2	-
14	0	35	-	67.9	-
15	1	35	-	68.2	-
16	17	112	-	69.6	-
17	145	184	44.8	69.0	24.2
18	283	63	44.8	?	-
19	495	153	44.8	68.8	24.0
20	903	312	45.0	68.8	23.8
21	459	386	44.6	69.0	24.4
22	211	321	44.4	68.4	24.0
23	47	212	44.2	69.3	25.1

continued on next page

Box №	n ('410')	n ('660')	$t_{Ps,410}$ [s]	$t_{Ps,660}$ [s]	($t_{Ps,660}$-$t_{Ps,410}$) [s]
24	0	62	-	68.0	-
25	0	32	-	69.0	-
26	17	87	-	69.8	-
27	124	100	44.6	67.8	23.2
28	194	62	44.6	69.2	24.6
29	263	7	44.2	-	-
30	356	63	44.6	68.2	23.6
31	404	152	45.4	68.8	23.4
32	123	210	44.6	69.2	24.6
33	17	135	-	70.0	-
34	0	47	-	68.8	-
35	4	16	-	-	-
36	7	47	-	70.2	-
37	44	29	45.4	70.0	24.6
38	42	9	45.0	-	-
39	29	29	44.8	70.4	25.6
40	40	29	45.0	71.0	26.0
41	31	72	45.6	70.0	24.4
42	1	32	-	69.6	-
43	0	20	-	-	-

7.3 Discussion

The obtained delay times for the signals from the '410' and '660' were compared with the delay times predicted by the reference model *IASP91*, which are approximately 44.1 s and 68.1 s, respectively. The differences between measured delay time and predicted delay time are plotted in Figures 7.7 and 7.8 for the '410' and '660', respectively.

The distribution of delay time differences for the **410-km discontinuity** generally displays a slight increase in delay times from north to south. The largest values are obtained below the northern Austrian Alps and Alpine foreland (+0.7 to +1.5 s within boxes 37-41). However, the data coverage of these southernmost boxes (boxes 37-41) is not very dense, making the results less reliable. In the north and northeast of the covered area (boxes 3-12 and 23), there is no difference in delay time to the *IASP91* reference model. However, box 10 (+1.5 s) is an exception with a striking contrast to box 9 (-0.1 s). As in both boxes data is densely spaced, the measured values are considered to be reliable. One possibility to explain such strong differences could be the distribution of piercing points within the box. However, the piercing points of the 410-km discontinuity in box 9 cluster in the southeast of the box and those of box 10 in the southwest (Figure 7.7), making it implausible that the piercing points should sample two completely separate regions. As the signals of *Ps* conversions from the upper mantle discontinuities are very weak themselves, the most probable explanation is that some particularly noisy traces or a scatterer strongly influence the sum trace although so many traces were stacked.

The uncertainty introduced by picking of the delay time of the signal is ±0.1 s, the uncertainty introduced by bandpass filtering is ±0.1 s (derived by filtering tests). Obviously the uncertainty introduced by noise depends on the number of stacked traces but can still not easily be estimated as the above discussion about boxes 9 and 10 shows. If an

uncertainty of ±0.2 s for boxes with at least 25 traces is assumed, the overall uncertainty amounts to ±0.4 s for a delay time value of mantle discontinuities within an individual box.

The sum trace in Figure 7.5 shows a delay of +0.7 s compared to the *IASP91* reference model. As the sum trace is stacked of more than 5500 individual traces, the uncertainty introduced by random noise should be negligible, so that delay time values of the mantle discontinuities in the sum trace is ±0.2 s.

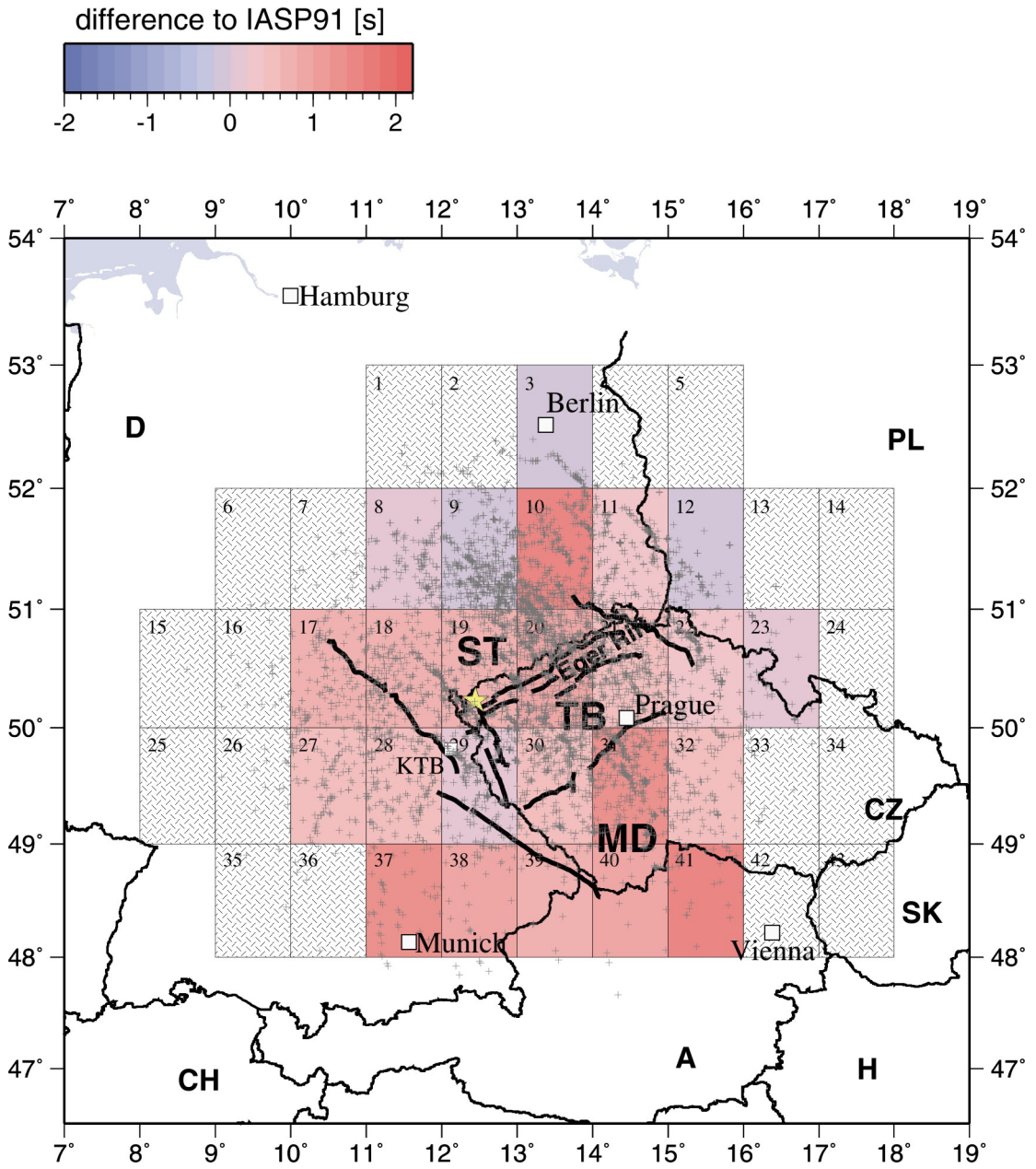

Figure 7.7: Difference between measured and theoretical delay time for the 410-km discontinuity. Red colours show longer and blue colours shorter delay times than predicted by the *IASP91* reference model, which could correspond to hot and cool temperatures near the discontinuity, respectively. Values vary between -0.1 s (boxes 3, 9,12) and +1.5 s (boxes 10, 41), the average is +0.7 s.

The **discontinuity at 660 km depth** does also show a deepening trend towards south (Figure 7.8). This effect is strongly reinforced by the values measured in the southernmost boxes 36-42 (+1.5 s to +2.9 s in relation to *IASP91*), which represent the area beneath the northern Alps and Alpine foreland. These boxes are not very well covered by data. However, as they show a coherent behaviour, the trend is assumed to be real. The delay time increase in these boxes is even stronger than the increase obtained for the same boxes for the 410-km discontinuity (see above).

In the majority of the boxes in the northern and central part of the area, the delay time of the *Ps* conversion from the '660' corresponds well with the value predicted by the *IASP91* model or is only slightly higher.

Again, there are some striking contrasts between neighbouring boxes. Mostly they occur at the margins, where the data coverage is less dense. Therefore it is suggested that these strong contrasts are caused by noise in the individual traces that could not be eliminated by stacking. The estimated uncertainty of the measured delay time values of the *Ps* conversion from the '660' is again ±0.4 s for the sum traces of individual boxes.

The sum trace in Figure 7.6 shows a delay of +0.5±0.2 s of the *Ps* conversion from the '660' compared to the *IASP91* reference model.

Geissler et al. (2005) found delays of the *Ps* conversion signals from the '410' and '660' in the investigation area of up to 2 s compared to *IASP91*. This is somewhat higher than the values found for most boxes in this thesis. Only in the southernmost boxes for the '660', larger values are found in the present study. However, *Geissler et al.* (2005) used less data and stacked the data stationwise and not according to boxes as in the present study. As most of the data used by *Geissler et al.* (2005) are included in the investigation of the mantle transition zone in this thesis, the values obtained here should be more reliable.

A receiver function investigation by *Grunewald et al.* (2001) showed no deviations of the depth of the '410' and '660' in the area investigated in this thesis and therefore supports the results found here. However, in the northern Austrian Alps and south Germany, where in this thesis longer delay times of the *Ps* conversions from the '410' and '660' are observed, *Grunewald et al.* (2001) also did not find any anomalies. Their study focused deeper on the Eifel volcanic region in the Rhenish massif of western Germany. This region is geologically comparable to the western Bohemian Massif as both are of Variscan origin and it is also overprinted by the European Cenozoic Rift system with its Tertiary and Quaternary volcanism and recent CO_2 emanations. The proposed plume beneath the Eifel volcanic region (*Ritter*, 2001) is further supported by *Grunewald et al.*'s findings of a 150 km wide and 20 km deep depression of the 410-km discontinuity in the upper mantle beneath the Eifel region. This is indicative of a zone of increased (by about 200 K) temperature and/or reduced seismic velocities in the mantle above 400 km depth. As such a feature cannot be found in this thesis, there is no hint to a comparable temperature or velocity anomaly beneath the western Bohemian Massif.

No indication for an anomaly of the '660' was found under the Eifel, which argues against a thermal anomaly at the bottom of the mantle transition zone (*Grunewald et al.*, 2001). The same is the case for the '660' beneath the western Bohemian Massif investigated in this thesis.

It is necessary to point out that structures significantly smaller than 150 km laterally can not be resolved by the receiver function method. The 1 s isochrones at 410 km depth have a diameter of comparable size (200 km).

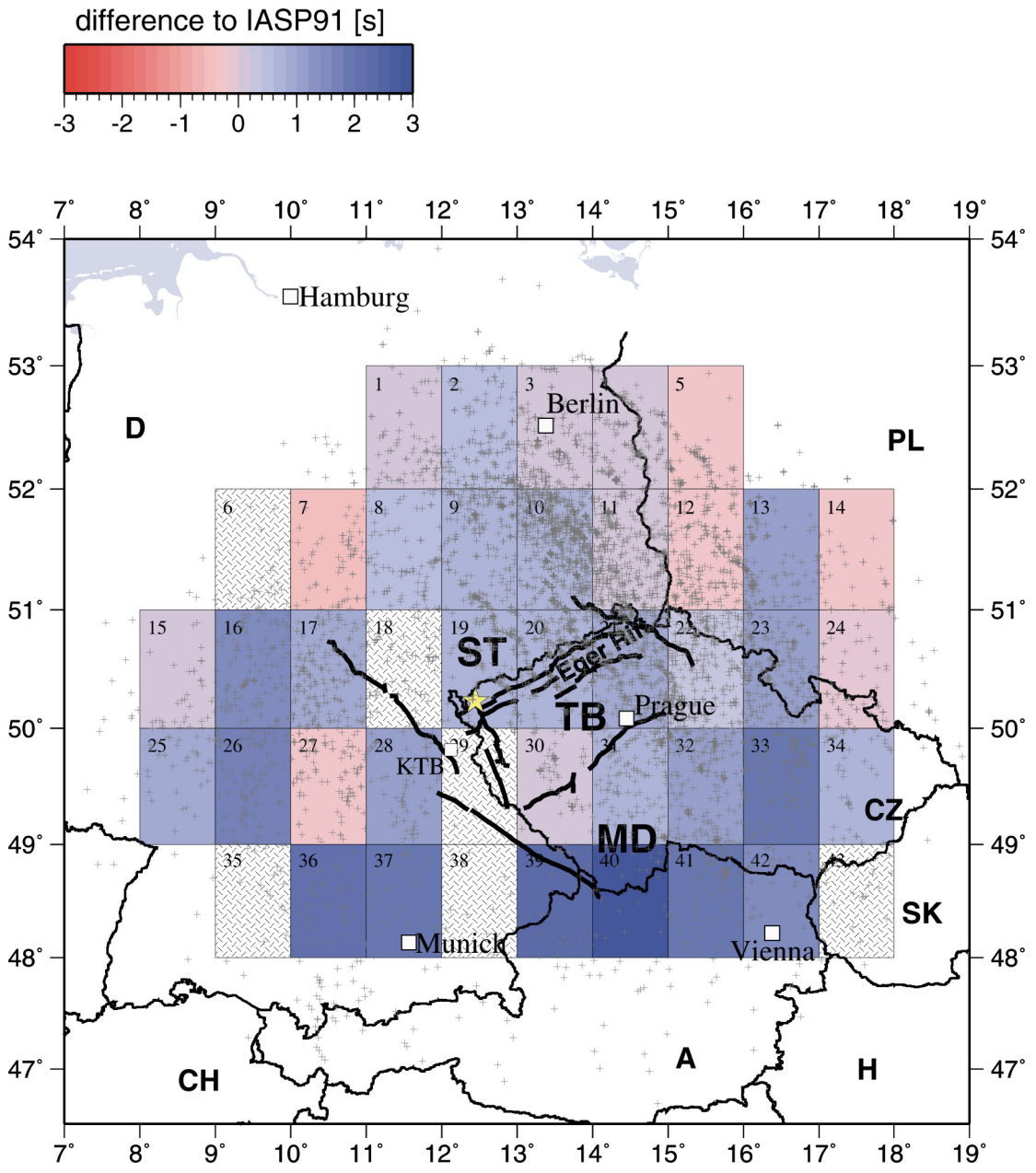

Figure 7.8: Difference between measured and theoretical delay time for the 660-km discontinuity. The colour scale is opposite to the scale in Figure 7.7 as the 660-km discontinuity has a negative *Clapeyron* slope d*P*/d*T*. Blue colours show longer and red colours shorter delay times than predicted by the *IASP91* reference model, which could correspond to cool or hot temperatures near the discontinuity, respectively. Values vary between -0.5 s (box 7) and +2.9 s (box 40), the average is +0.5 s.

An important value for discussion of temperature variations within and above the mantle transition zone is the delay time difference between the two discontinuities (*Li et al.*, 2003b), which is a good estimate of the **thickness of the mantle transition zone**. As the '410' and '660' have opposing *Clapeyron* slopes, a temperature increase across the mantle transition zone would reduce the distance between the two discontinuities, while a temperature decrease would increase the distance between them. If a temperature anomaly occurs in the uppermost mantle above the mantle transition zone, the delay times of both

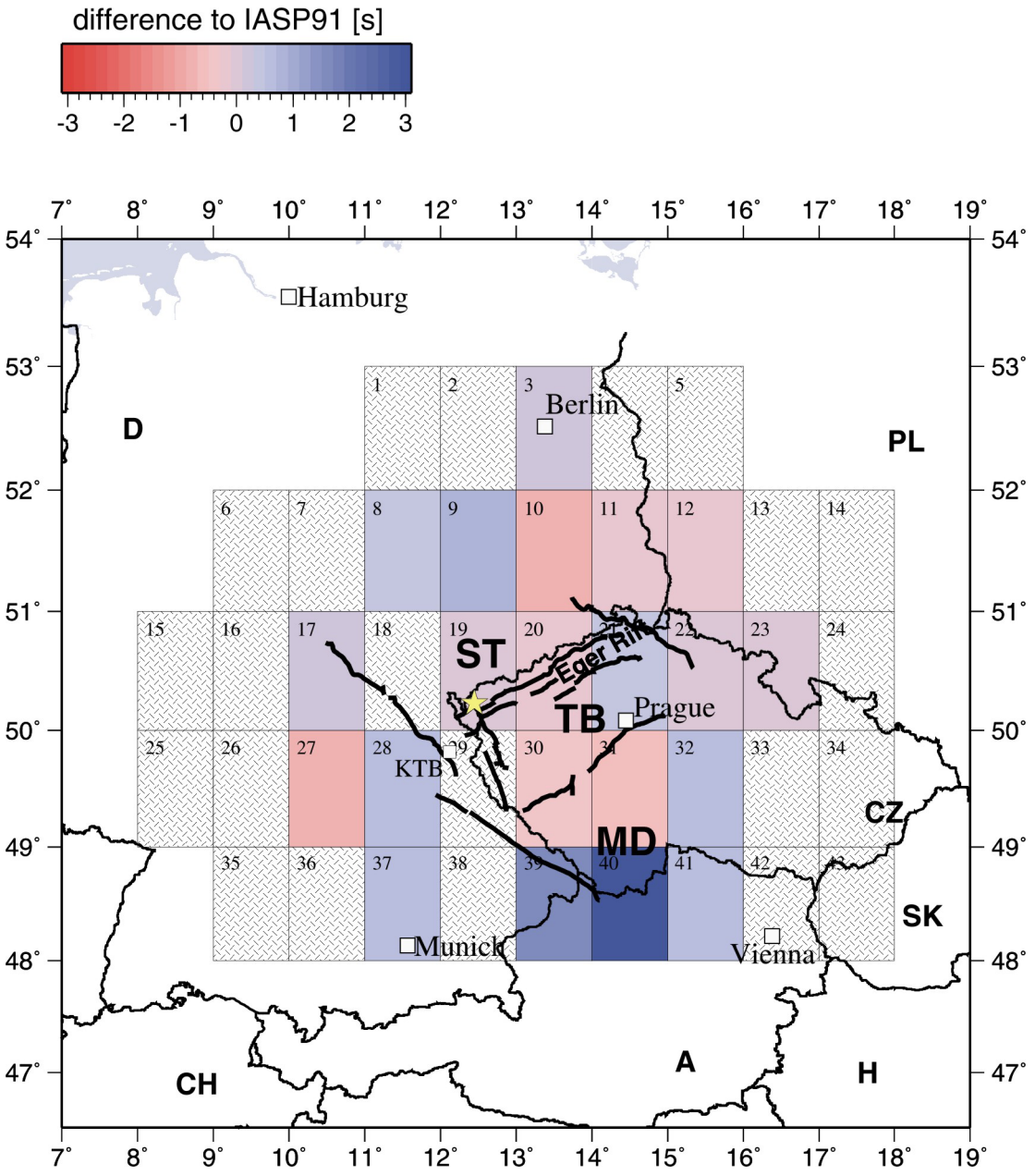

Figure 7.9: The difference of the delay times between the *Ps* conversions from the '660' and the '410' is predicted to be 24.0 s by the *IASP91* reference model. This value was subtracted from the measured delay time difference of the two discontinuities and plotted into this map. Blue colours indicate a thicker, red colours a thinner mantle transition zone than predicted by *IASP91*. The values within the boxes vary between -0.8 s (boxes 10, 27) to +2.0 s (box 40). Coverage with piercing points is not shown because it is different for the two discontinuities within one box.

discontinuities would be affected in the same direction while the time difference between them remains constant.

The difference between the measured delay time difference and the theoretical one predicted by *IASP91* (24.0 s) is shown in Figure 7.9. The values vary between -0.8 s (boxes 10, 27) to +2.0 s (box 40). These extreme values appear in boxes that already showed extreme behaviour for either the '410' or the '660' as described above. The other boxes show mostly smaller values and no trend or coherent structure can be postulated.

Therefore it is concluded that the generally very small positive and negative differences to the *IASP91* reference model measured in the investigated area are mainly due to noise. Hence the overall thickness of the mantle transition zone in the investigation area corresponds to the thickness given by the *IASP91* reference model (250 km). Only in the southernmost area beneath the northern Alps and Alpine foreland, there is a trend of thickening of the mantle transition zone. It is caused by an increase of delay times of both *Ps* conversions from the 410- and 660-km discontinuities with a relatively stronger increase for the '660'.

For the northern and central part of the area covered by data, the good agreement between measured and predicted delay times differences of the 410- and 660-km discontinuities points to normal temperatures of the mantle transition zone in this area. As both phases are slightly delayed compared to the *IASP91* reference model (+0.7±0.2 s and +0.5±0.2 s for the '410' and the '660', respectively), this points to decreased *S* wave velocities in the upper mantle above the mantle transition zone. The *IASP91* reference model contains no low velocity zone representing the asthenosphere. The existence of an asthenosphere with an increased v_p/v_s ratio beneath the investigated area could explain at least some part of the increased delay times of the '410' and '660' with respect to the reference model.

If the manifold processes that point to magmatic activity beneath the western Bohemian Massif should have their origin in a diapiric mantle upwelling as predicted by *Granet et al.* (1995), the absence of a distinct topography of the upper mantle discontinuities leads to the conclusion that this predicted mantle finger does not show an imprint on the upper mantle discontinuities. If it exists, it either needs to have its origin well above the mantle transition zone, or its diameter is significantly smaller than 150 km at the depth of the mantle transition zone and thus too narrow to be resolved by teleseismic receiver functions.

At 54.4 s delay time after the *P* onset, a weak positive phase is visible in the sum trace as well as in the individual boxes of the *P* receiver functions (Figures 7.5, 7.6), that can be attributed to the **520-km discontinuity**. As calculations of synthetic receiver functions by *Geissler* (2004) from earth models without a velocity discontinuity at 520 km depth do not show any artefacts that could be mistaken for a discontinuity, it seems very probable that the observation of a '520' in the investigated area is reliable. However, the phase was not analysed in more detail. Therefore, scattered phases or effects of deconvolution that might have led to an artificial occurrence of this phase can not be completely ruled out.

Several studies show a low velocity zone on top of the 410-km discontinuity (e.g. *Song et al.,* 2004; *Gilbert et al.,* 2003; *Vinnik et al.,* 2003; *Revenaugh and Sipkin,* 1994; *Nolet and Zielhuis*, 1994). *Bercovici and Karato* (2003) present a model of the Earth's mantle which predicts the presence of a layer of melt or partial melt above the 410-km discontinuity of the order of less than 10 km. However, the data used in the present study

does not show a coherent phase atop the 410-km discontinuity. Only very few non-coherent boxes (e.g. boxes 08, 17, 37-39) show a strong negative phase in front of the *P*-to-*S* conversion from the '410'. This indicates that the low velocity layer predicted by *Bercovici and Karato* (2003) is probably not a global feature. This is in agreement with *Huang et al.* (2005), who infer that the water content in the mantle transition zone varies regionally and that therefore the low velocity zone on top of the '410' should be a regional feature, too.